Check for updates

Advanced Functional Materials

ADVANCED FUNCTIONAL MATERIALS
www.afm-journal.de

RESEARCH ARTICLE OPEN ACCESS

Coating Artificial Spider Silk Fiber with Magnetic FeCo: An Effective Strategy for Creating a Flexible Magneto-Responsive Material

Filippo Lanaro[1] | Federico Spizzo[1] | Gabriele Greco[2,3] | Benjamin Schmuck[2] | Anna Rising[2,4] | Lucia Del Bianco[1]

[1]Department of Physics and Earth Science, University of Ferrara, Ferrara, Italy | [2]Department of Animal Biosciences, Swedish University of Agricultural Sciences, Uppsala, Sweden | [3]Department of Civil Engineering and Architecture, University of Pavia, Pavia, Italy | [4]Department of Medicine Huddinge, Karolinska Institutet, Neo, Huddinge, Sweden

Correspondence: Federico Spizzo (federico.spizzo@unife.it) | Gabriele Greco (gabriele.greco@unipv.it)

Received: 13 February 2026 | **Revised:** 10 April 2026 | **Accepted:** 25 April 2026

Keywords: artificial spider silk fibers | magnetic polymer composites | magneto-responsive materials | magnetostrictive FeCo | mechanical tensile testing | metallic coating | MOKE magnetometry

ABSTRACT

Combining spider silk and magnetic nanostructures is a key challenge for advancing technological fields such as soft robotics, magnetosurgery, and smart textiles. It is essential to devise approaches that also aim to expand fundamental knowledge on the feasibility of coupling the protein-based fiber with the inorganic magnetic phase. An original strategy is presented to create magneto-responsive artificial spider silk fibers by coating them with thin layers (nominal thickness 5nm, 10nm, and 100nm) of ferromagnetic and magnetostrictive FeCo alloy via sputtering deposition. The mechanical strength and elasticity of the produced fibers remain close to those of the uncoated material. A relationship is established between the magnetic properties of the FeCo coating and its structural characteristics, which are strongly influenced by the underlying fiber morphology. The magnetomechanical response of the FeCo coating of single fibers under strain is evaluated using magneto-optical Kerr effect magnetometry. Experimental data, interpreted through the shear-lag model, reveal excellent silk-metal coupling and highlight how the coating thickness governs stress transmission and the fragmentation process. The reversibility of the magnetomechanical response is investigated, providing further insights into the silk/metal coupling. These findings contribute to clarifying how the interplay between organic and inorganic components determines the composite's overall properties.

1 | Introduction

The growing interest in green and sustainable smart materials has recently stimulated research efforts on a particular class of composite systems, obtained by combining a natural biopolymer and an inorganic phase, usually in the form of micro- or nanoparticles, which act as matrix and filler, respectively [1–6]. In the designed composite, the biopolymer should ensure biocompatibility, controllable biodegradability, lightness, and mechanical softness along with strength, while the inorganic phase provides additional functionality, such as responsiveness to a magnetic or electric field [7–10] optical activity [11, 12] or antimicrobial properties [13, 14].

In this context, endowing native spider silk fibers – a protein-based material renowned for its strength, flexibility, and toughness [15–19]– with magnetic functionality is an extremely advantageous prospect. Indeed, such a composite system is expected to

This is an open access article under the terms of the Creative Commons Attribution License, which permits use, distribution and reproduction in any medium, provided the original work is properly cited.
© 2026 The Author(s). *Advanced Functional Materials* published by Wiley-VCH GmbH

have significant potential for application in various fields, such as bio-engineering and soft robotics [20–22], magnetosurgery [23, 24], and in smart textile technology [25–27]. After the first attempts in this direction by Mayes et al., who in 1998 succeeded in preparing natural spider silk fibers with a dense surface layer of iron oxide nanoparticles [28], no significant progress was made for many years, underscoring the complexity and ambition of the goal. Only very recently, Kryuchkova et al. have shown that, by injecting magnetic nanoparticles into the silk gland of the spider, a composite fiber is produced by the animal [29]. The method is interesting but seems impractical for large-scale production of the material. We used a very different strategy to obtain natural spider fibers with magnetic properties, namely coating them with a 100nm thick FeCo layer by sputtering deposition [30]. A main drawback of this approach is the reduced availability of natural material. Moreover, native spider fiber consists of a variable number of intertwined filaments [30, 31], which results in a peculiar morphology of the magnetic coating and makes it extremely difficult to obtain composite samples with a good degree of reproducibility of the magnetic properties.

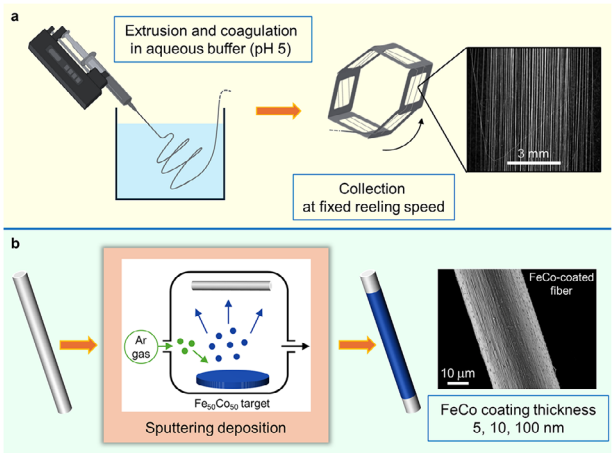

FIGURE 1 | Schematic representations: (a) wet spinning of the artificial spider silk fiber; (b) subsequent sputtering deposition of the magnetic FeCo coating on the fiber (a typical scanning electron microscopy image of a fiber with a 100nm thick coating is also shown, see Section 2.5).

However, these limitations can now be addressed thanks to major advances in the production of recombinant spider silk proteins using diverse heterologous expression systems (e.g., bacterial, yeast, mammalian, and insect cells) [32, 33]. Furthermore, efficient methods for processing the proteins into continuous artificial fibers with good mechanical performance have been developed [34–37].

For instance, we recently reported on the successful production of artificial spider silk fibers made of a small genetically engineered spider silk protein (NT2RepCT, so-called minispidroin [38, 39]), with embedded magnetite nanoparticles [40, 41]. In particular, by providing the nanoparticles with a hydrophilic coating that favored their homogeneous dispersion in the protein matrix, it was possible to produce hundreds of meters of continuous fiber, with ductility comparable to that of the pristine material even at high magnetite loading (up to 20 wt.%, corresponding to ~7 vol.%). Especially in potential applications involving close interaction with biological entities, the incorporation of the nanoparticles into the fiber is a step forward compared to anchoring them to the surface, because it reduces the risk of detachment. Moreover, in the case of embedded superparamagnetic nanoparticles, the magnetic response of the composite fiber can be switched on and off by an external magnetic field. However, to bring an array of superparamagnetic nanoparticles to magnetic saturation, a high magnetic induction field, on the order of 1 Tesla, is required [42–44], which may be an issue for magnetic actuation applications.

To produce magnetic spider silk fibers that saturate under a moderate magnetic field or that retain a high magnetization like a permanent magnet, a very attractive strategy is the sputtering deposition of a magnetically soft or hard coating, respectively. This approach was used to prepare composite silk fibroin films that, thanks to a thin soft ferromagnetic coating constituting a volume fraction below 0.1%, can be magnetically actuated using a small permanent magnet [45]. In principle, using masks, one could design the desired coating pattern, which would lead to improved motion and shape morphing capabilities. Moreover, the method offers the possibility of making the fiber electrically conductive with a metallic coating, thus paving the way to a transition from traditional to soft and sustainable electronics [46, 47]. Another fascinating prospect is to use a magnetostrictive coating in order to obtain spider silk fibers with both magnetic functionality and stress sensitivity [30]. This strategy could indeed allow for significant progress, but the topic is still almost completely unexplored, and further research efforts are needed to first tackle a fundamental question: given the strong chemical and mechanical contrast between the artificial protein-based fiber and the inorganic magnetic/magnetostrictive coating, is it really possible to combine them while preserving their specific properties?

To address this issue, we conducted a systematic study on artificial spider silk fibers coated with a FeCo layer of different nominal thicknesses (5nm, 10nm and 100nm) by dc magnetron sputtering (Figure 1). The fibers were based on the mini-spidroin $(A_3I)_3$-A_{14}, which is an engineered variant of NT2RepCT [35]. The FeCo alloy was chosen because of its high saturation magnetization, superior to that of any other ferromagnetic material, low magnetocrystalline anisotropy, and positive magnetostriction [48, 49]. Here, we demonstrate that we have produced fibers with magnetic and magnetomechanical responsiveness, while preserving the mechanical performance of the uncoated material to a satisfactory extent. The magnetic study, complemented by scanning electron microscopy, allowed us to clarify how the FeCo metal layer grows on such a particular type of substrate, namely the polymer fiber, and to what extent its magnetic properties are influenced by the geometry and surface morphology of the fiber itself. The analysis of the magnetic hysteretic behavior of the samples subjected to mechanical strain was effectively used to probe the degree of coupling between fiber and FeCo coating.

Overall, this study takes a step forward toward creating smart, sustainable materials with magnetic functionality by exploring a new path that leverages the coupling of protein-based artificial fibers with inorganic magnetic nanostructures in the form of thin metal coatings.

16163028, 2026, 48, Downloaded from https://advanced.onlinelibrary.wiley.com/doi/10.1002/adfm.75699 by Universita Di Ferrara, Wiley Online Library on [23/06/2026]. See the Terms and Conditions (https://onlinelibrary.wiley.com/terms-and-conditions) on Wiley Online Library for rules of use; OA articles are governed by the applicable Creative Commons License

2 | Materials and Methods

2.1 | Production of the Artificial Spider Silk fiber

The minispidroin $(A_3I)_3$-A_{14} was expressed in *E. coli* in a bioreactor, and purified in native conditions using affinity chromatography, as described previously [35]. After purification, the mini-spidroins, stored in 20 mM TrisHCl buffer (pH 8), were concentrated to 300 mg mL^{-1} with a stirred cell device (Merck), using a 10 kDa cutoff membrane, at 4°C, and using pressurized N_2 up to 4 bar. The concentrated protein solution (the spinning dope) was extruded at ambient temperature through a tapered A-150250000SA-B278 nozzle (Tecdia) with a 150 µm outlet diameter into an 80 cm long bath filled with 0.75 M acetate buffer at pH 5 (Figure 1a). The spinning dope was delivered at a constant flow rate of 45 µL min^{-1}.

Upon extrusion, the spinning dope immediately solidified, and the fiber was gently guided onto a rotating collection wheel, which transferred it into a second bath containing the same acetate buffer. Following this step, the fiber was continuously collected in air at velocities of up to 35 cm s^{-1}. The collected fibers were subsequently stored in a drying chamber maintained at a relative humidity below 20%.

As explained in the following Section 2.2, the sputtering deposition technique involved as a first step the insertion of the substrate (in our case, the polymer fiber) into the deposition chamber under high vacuum. Therefore, we prepared control samples by exposing as-prepared fibers to a high vacuum stage comparable to that used during the sputtering procedure, i.e., they were kept at 5×10^{-5} Pa for about 100 min.

2.2 | Sputtering Deposition

The spun fibers were coated with $Fe_{50}Co_{50}$ (FeCo) alloy using a custom-made high-vacuum magnetron sputtering apparatus produced by Rial Vacuum (now SAES Rial Vacuum) (Figure 1b). The high-purity (99.95%) FeCo equiatomic sputtering target (Testbourne Ltd) was mounted on a dc sputtering source. The plasma discharge was driven by setting the Ar pressure and the current discharge to ∼0.26 Pa and 0.2 A, respectively, and, in these conditions, the discharge power was 75 W. The base pressure of the sputtering apparatus was $\sim 5 \times 10^{-5}$ Pa. The corresponding sputtering rate was equal to 0.18 nm s^{-1} and was measured using a quartz microbalance system based on 6 MHz gold-plated crystal, a Vaqtec oscillator kit, and an MS-9150 Metex Universal System.

Pieces of the as-prepared fiber, about 10 mm long, were each fixed on a different cardboard frame. The frames were then laid on a sample holder, so as to expose one side of the fibers to the flux of sputtered atoms. Then, the frames were rotated to expose the opposite side and thus complete the coating process of the fibers, taking care to leave a few millimeters uncoated near the ends for ease of handling. In particular, for the study of the mechanical properties, only the central 3 mm of the fibers were coated to ensure correct clamping during the tensile tests without the risk of breaking the FeCo layer and damaging the polymer. During the deposition, the sample holder was rotated to improve the coating homogeneity. Coating the fibers on both sides implied an overall permanence in vacuum conditions of about 100 min.

We prepared samples with different nominal thicknesses of the FeCo coating: 5nm, 10nm, and 100nm. For each thickness, we prepared a batch of 50 pieces of fiber. In the following text, we will use the expression "5nm fiber" to refer to a sample with 5nm thick FeCo coating, and similarly for samples with FeCo coating 10nm and 100nm thick. For each batch of fibers with a given FeCo thickness, a reference (REF) film was also prepared by depositing a FeCo layer with the same thickness on a planar, naturally oxidized, silicon substrate.

2.3 | Light Microscopy

Fiber diameters were measured at five randomly selected points using light microscopy (Zeiss Microscope Axioscope 5/7 KMAT). The averaged values were calculated following previously described procedures [16].

2.4 | Birefringence Analysis

The birefringence index was measured using a Zeiss Axioscope 5/7 KMAT microscope equipped with a polarizer and a tilting Berek compensator (5λ). The birefringence index of the fibers was calculated by dividing the measured retardation of polarized light by the fiber thickness, approximated by the fiber diameter.

2.5 | Scanning Electron Microscopy Analysis

Scanning Electron Microscopy (SEM) observations were performed using a FEG SEM Zeiss Gemini 460, also equipped for analysis in variable-pressure mode. The FeCo-coated fibers to be investigated were attached on stubs for SEM with conductive carbon adhesive tape.

2.6 | Mechanical Testing

All fibers were tested at room temperature and 25%–30% relative humidity (RH). Each single fiber was mounted on a paper frame with a (7.5×7.5) mm^2 open square window providing an effective gauge length of ∼7.5 mm. Of this length, ∼3 mm corresponded to the coated region and ∼4.5 mm to the uncoated region, with mechanical gripping applied exclusively to the uncoated ends. Tensile tests were performed using an Instron Single Column 5943 equipped with a 5N load cell at a strain rate of 6 mm min^{-1}. Engineering stress was calculated under the assumption of a circular cross-section. From the resulting engineering stress–strain curves, Young's modulus was determined by linear regression over the initial elastic region (up to 2% strain), strength was taken as the stress at fracture, and toughness modulus was calculated as the area under the curve. A minimum of ten fibers of each type were tested. Statistical analysis was carried out using a single one-tailed pairwise ANOVA with Excel.

Stress relaxation tests were conducted using the Instron Single Column 5943. The fibers were stretched at a strain rate

16163028, 2026, 48, Downloaded from https://advanced.onlinelibrary.wiley.com/doi/10.1002/adfm.75699 by Universita Di Ferrara, Wiley Online Library on [23/06/2026]. See the Terms and Conditions (https://onlinelibrary.wiley.com/terms-and-conditions) on Wiley Online Library for rules of use; OA articles are governed by the applicable Creative Commons License

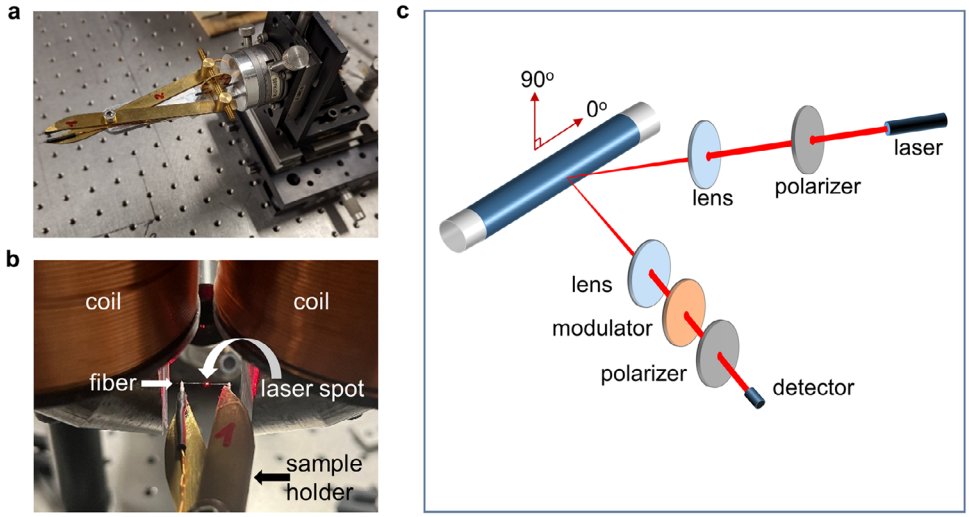

FIGURE 2 | (a) Custom-made sample holder used for MOKE analysis. (b) The picture shows a FeCo-coated fiber mounted between the two arms of the sample holder; in this configuration, the magnetic field, produced by a pair of coils, is parallel to the long axis of the fiber (0° direction). (c) Scheme of the MOKE apparatus for the analysis of the FeCo-coated fibers; the 0° and 90° directions along which the magnetic field was applied are indicated.

of 6 mm min^{-1} until reaching 2% engineering strain and then held at that strain for 20 min to allow relaxation. The strain was subsequently increased to 4% at the same rate, followed by another 20-min relaxation period. This procedure was repeated in 2% increments up to a maximum strain of 20%.

2.7 | Magnetic Analysis Methods

2.7.1 | Superconducting Quantum Interference Device (SQUID) Magnetometry

Magnetic measurements were carried out using a Quantum Design MPMS-XL SQUID magnetometer equipped with the reciprocating sample option (RSO) mode (maximum applied field 4 MA m^{-1}, sensitivity 10^{-10} A m^2). The saturation magnetization of the REF films was calculated by dividing the measured magnetic moment by the volume of the magnetic FeCo layer. The area of the samples was evaluated using the ImageJ software [50], while their thickness was taken equal to the nominal one (i.e., 5nm, 10nm, and 100nm).

Samples of coated fibers were prepared by placing a precise number of them between two pieces of adhesive tape, trying to align them parallel.

2.7.2 | Magneto-Optical Kerr Effect (MOKE) Magnetometry

For the MOKE analysis, each FeCo-coated fiber was fixed to the arms of the custom-made device, shown in Figure 2a,b, using silver conductive paint. The sample holder was anchored to a rotation stage, allowing us to change the orientation of the fiber with respect to the applied magnetic field H. Moreover, an endless screw allowed to increase the distance between the two arms of the sample holder, so as to impart a tensile strain to the fiber.

The measurements were performed in longitudinal configuration with the polarization modulation technique (Figure 2c), using p-polarized light produced by a He-Ne laser (wavelength λ = 632.8 nm) [51]. As the fiber diameter (~30 μm) was very small with respect to the laser beam size (~1 mm), the incident beam was focused on the fiber, and the diffused light was then collimated on the detector using a lens. The reflected light passed through a photo-elastic modulator, which provided a polarization modulation at a frequency of 50 kHz, was filtered by a polarizer set at 85° with respect to the incident polarization, and then collected by the detector. We recorded both ellipticity and rotation, i.e., the contributions of the signal oscillating at 50 kHz and 100 kHz, respectively, which are proportional to the sample magnetization [52]. As they showed the same magnetic field dependence, only the ellipticity was considered, which displayed a higher signal-to-noise ratio. In the following, the ellipticity signal is reported as a function of H, as normalized to that measured at the magnetic saturation, which therefore corresponds to the normalized magnetization.

3 | Results and Discussion

3.1 | Microstructural Characterization

The as-prepared, vacuum-exposed, and FeCo-coated fibers were observed by light microscopy. They exhibited a characteristic longitudinal groove (Figure S1a–c), typical of wet-spun artificial spider silk fibers [16], and the mean diameter was ~30 μm (Figure S1d). We performed birefringence measurements on the as-prepared and vacuum-exposed fibers, a technique that can provide relevant information about molecular order in this type of material [53]. The birefringence index did not differ significantly in the two samples, indicating that the molecular order was not markedly affected by the exposure to high vacuum (Figure S1e).

The morphology of the FeCo-coated fibers was investigated by SEM. In particular, the 5nm fiber was analyzed in variable-

16163028, 2026, 48, Downloaded from https://advanced.onlinelibrary.wiley.com/doi/10.1002/adfm.75699 by Universita Di Ferrara, Wiley Online Library on [23/06/2026]. See the Terms and Conditions (https://onlinelibrary.wiley.com/terms-and-conditions) on Wiley Online Library for rules of use; OA articles are governed by the applicable Creative Commons License

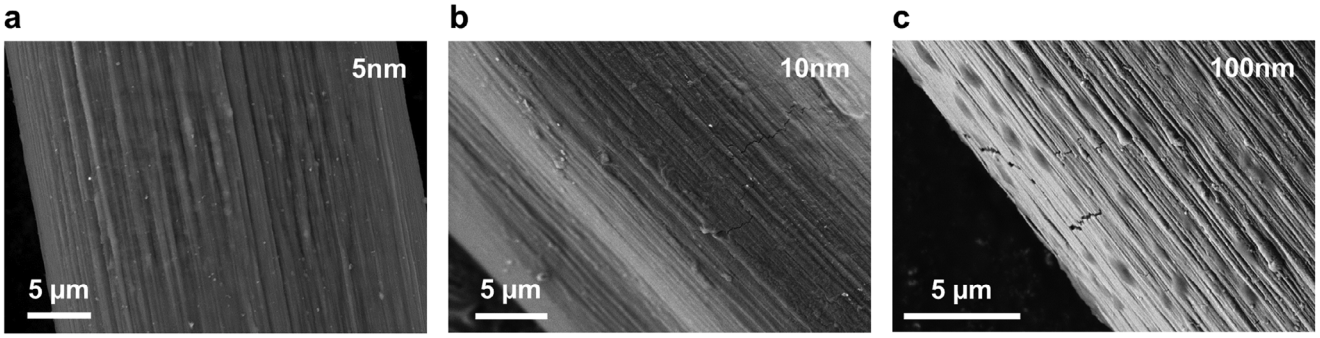

FIGURE 3 | Representative SEM secondary electron images of the FeCo-coated fibers. The image of the 5nm fiber was taken in variable-pressure mode.

pressure mode, while for the 10nm and 100nm fibers we carried out conventional SEM analysis, which allowed for better resolution (the FeCo coating itself made the samples electrically conductive). Representative images for each fiber type are displayed in Figure 3.

All the fibers present a corrugated surface characterized by ripples parallel to the long axis. The FeCo coating provides a rather uniform contrast; however, the presence of cracks is well detectable in the 10nm and 100nm fibers, originating from the relief of strong built-in stresses accumulated during the sputtering process. This initial cracking is favored by the corrugated surface of the silk substrate, where the natural ripples act as nucleation sites for localized fracturing.

Electric measurements of voltage vs. current (V–I) on a set of 10nm fibers confirmed that they were conductive and had ohmic behavior, in line with previous observations (Figure S2) [30]. However, electrical resistance values over a wide range were measured in the different samples (from kΩ to hundreds of kΩ), indicating the irregular presence of cracks.

3.2 | Mechanical Properties

The mechanical properties of the fibers were investigated through tensile testing (Figure 4 and Figure S3). The strain at break of the vacuum-exposed fibers is comparable to that of the as-prepared ones (Figure 4a), indicating that the artificial silk we have produced is more resilient to vacuum conditions compared to native spider silk [30, 54]. Similarly, 5nm and 10nm fibers show no significant difference in strain at break compared to the controls. In contrast, 100nm fibers exhibit a markedly lower strain at break. This reduction may be attributed to the relatively thick FeCo coating, which likely increased the brittleness of the fibers without significantly affecting their strength. Indeed, the tensile strength of all fibers is similar (Figure 4b). The presence of the coating has an impact on the strain at break but not on the strength, as the stress–strain curves of the composite fibers are mostly flat beyond the yield point (Figure S3), i.e., the stress displays just a tiny increase over a significant strain interval. In the coated fibers, the Young's modulus is similar within the errors, and, in the 10nm and 100nm fibers, it is slightly but significantly higher than that of the uncoated samples (Figure 4c). Given the different stiffness of a metal and a polymer, the FeCo layer grown on the artificial spider silk fiber reasonably determines a small increase in the Young's modulus of the composite, compared to the uncoated material. The toughness modulus follows the same trend as the strain at break, as it depends on both the stress and the strain (Figure 4d). In general, these results demonstrate that the mechanical properties of the as-prepared material, which were in line with those previously reported for artificial spider silk fibers produced with a similar spinning protocol [35, 37], were maintained to a large extent in the coated samples, especially for low FeCo thickness values.

We investigated whether the metal coating had an impact on the viscoelastic behavior of the polymer fibers. For this purpose, stress relaxation tests were performed following the procedure schematized in Figure S4, to quantify the extent to which the fibers relaxed when held at specific strain levels. As shown in Figure 5, in all fibers the stress decreases substantially within the first 5 min; the stress values measured at 10 and 20 min are nearly identical in all samples. Hence, in both the as-prepared and coated fibers, most of the stress relaxation occurred during the initial 5 min.

3.3 | Magnetic Study of the FeCo-coated Fibers

3.3.1 | Magnetic Moment Measurements and Estimation of the FeCo Coating Effective Thickness

Measurements of magnetic moment were carried out by SQUID magnetometry at room temperature on three samples consisting of a precise number of FeCo-coated fibers (from 5 to 21, depending on the typology; see Table S1 and related information). For each sample, we calculated the total volume of the FeCo coating, considering its nominal thickness and a hollow cylindrical shape. Then, assuming that the saturation magnetization M_S of the FeCo phase was the same as that measured in the corresponding REF film (Table S1), we calculated the expected magnetic moment. Table S1 shows that, in all three samples, the measured moment is lower than the predicted one by a percentage that increases with decreasing the nominal FeCo thickness, which indicates that the volume of the FeCo phase was actually less than calculated. This is consistent with a low sticking coefficient of the FeCo on the polymer fiber during the sputtering process (i.e., the ratio of the number of adsorbed metal atoms to the total number of metal atoms arriving at the substrate [55, 56]), which affected

16163028, 2026, 48, Downloaded from https://advanced.onlinelibrary.wiley.com/doi/10.1002/adfm.75699 by Universita Di Ferrara, Wiley Online Library on [23/06/2026]. See the Terms and Conditions (https://onlinelibrary.wiley.com/terms-and-conditions) on Wiley Online Library for rules of use; OA articles are governed by the applicable Creative Commons License

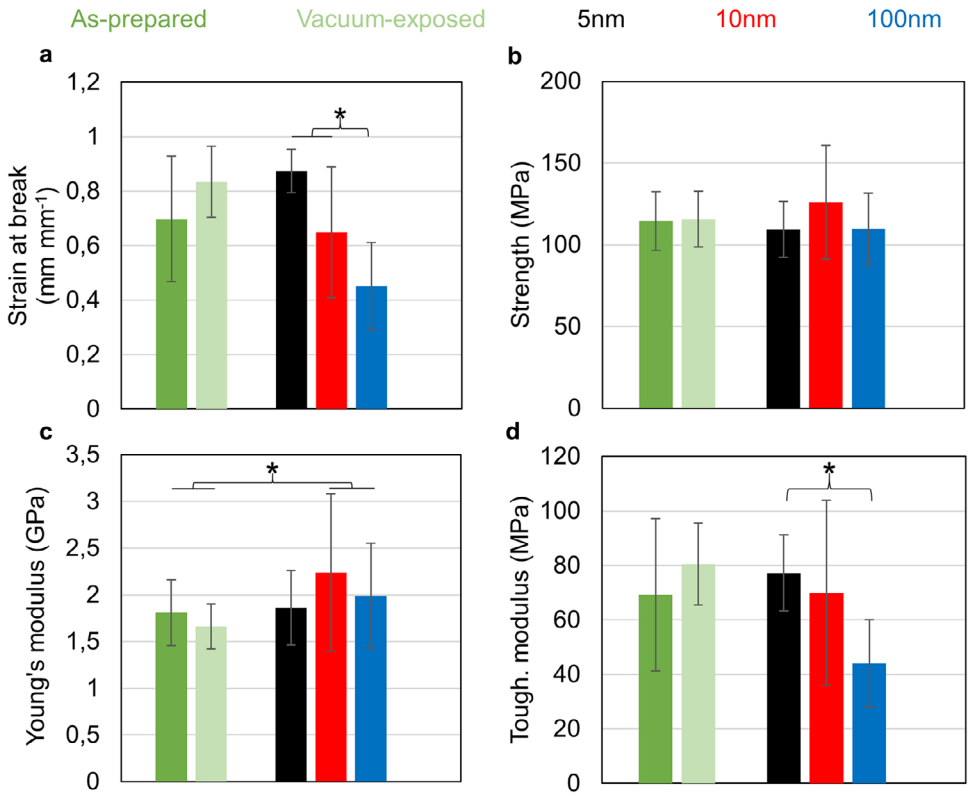

FIGURE 4 | Mechanical properties of the as-prepared, vacuum-exposed, and FeCo-coated fibers, obtained through tensile testing. (a) Strain at break, (b) strength, (c) Young's modulus, and (d) toughness modulus. The error bars represent the standard deviation. Stars indicate that the difference is significant (p-value<0.05).

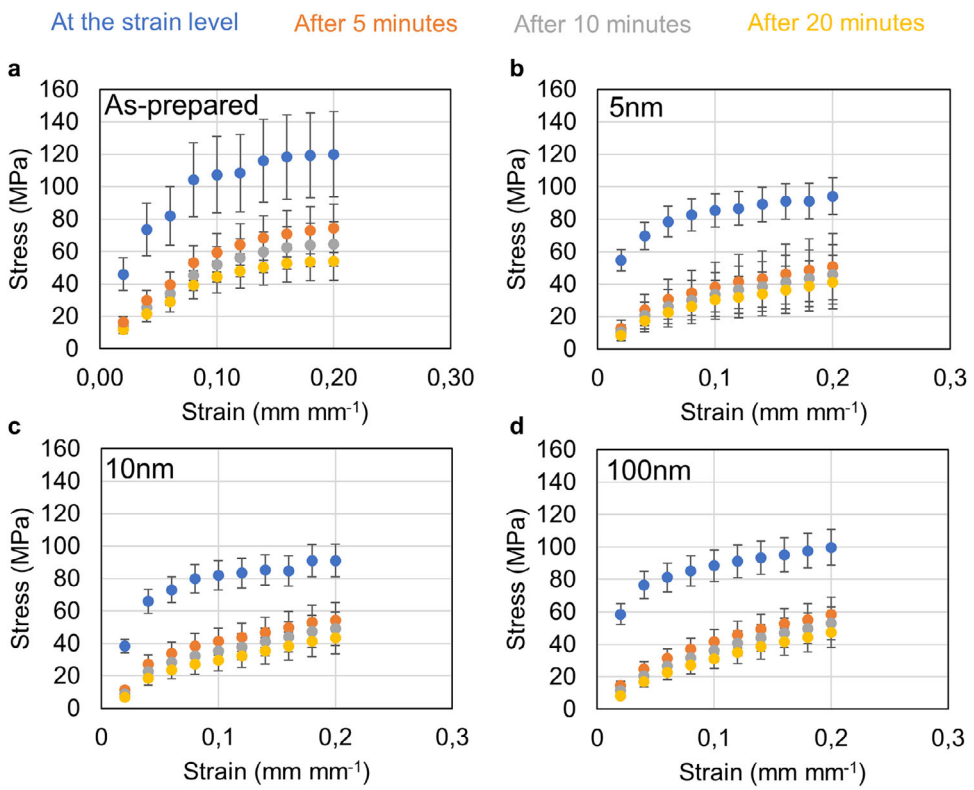

FIGURE 5 | Results of the stress relaxation tests carried out on the (a) as-prepared fibers, and the FeCo-coated ones: (b) 5nm, (c) 10nm, (d) 100nm. Stress levels of the fibers at different strain levels (blue dots), and measured after 5 (orange dots), 10 (gray dots), and 20 (yellow dots) minutes. The error bars represent the standard deviation.

16163028, 2026, 48, Downloaded from https://advanced.onlinelibrary.wiley.com/doi/10.1002/adfm.75699 by Universita Di Ferrara, Wiley Online Library on [23/06/2026]. See the Terms and Conditions (https://onlinelibrary.wiley.com/terms-and-conditions) on Wiley Online Library for rules of use; OA articles are governed by the applicable Creative Commons License

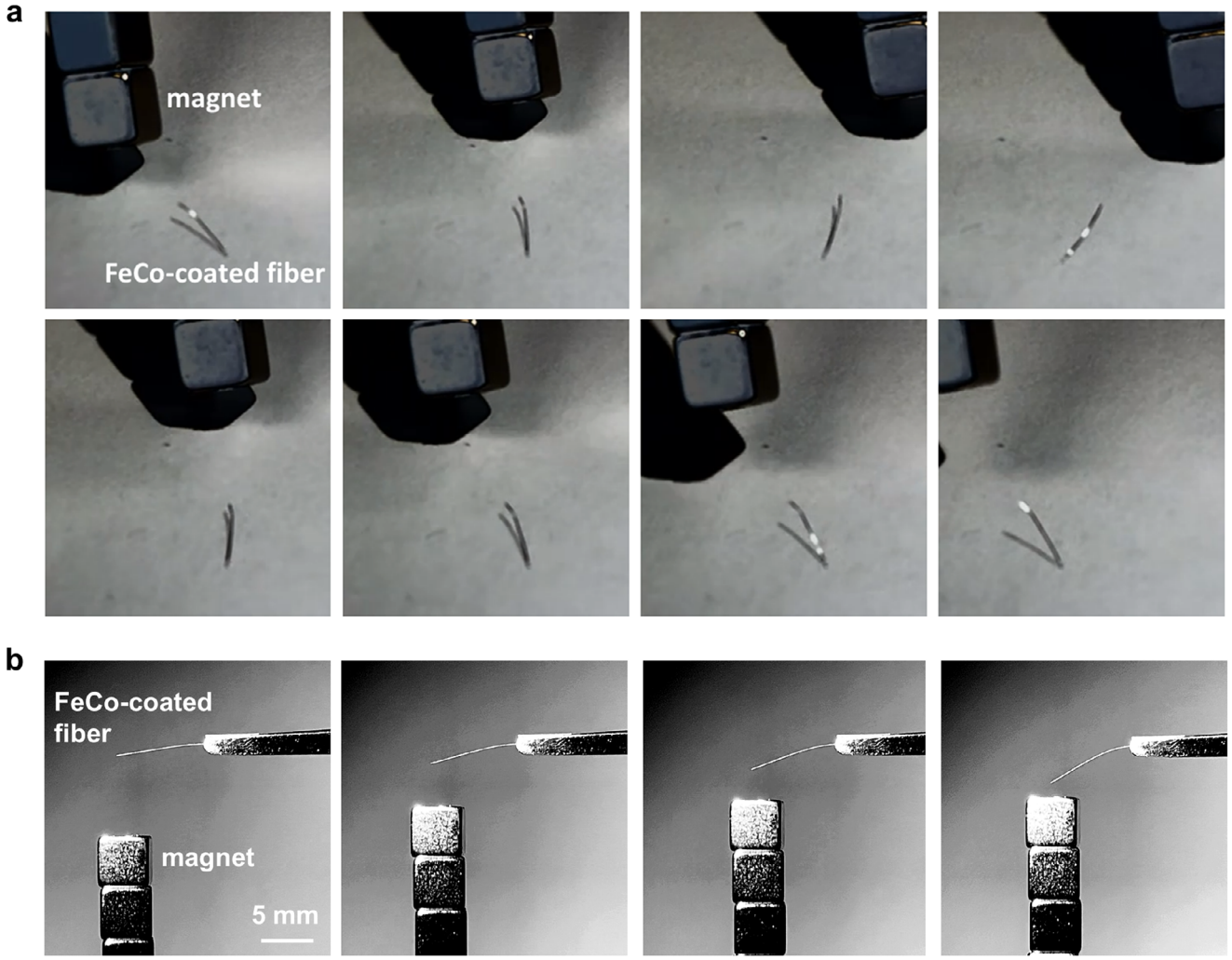

FIGURE 6 | (a) A 100nm fiber, glued at one end on a horizontal plane, is actuated by approaching a permanent magnet at a distance of ∼1 cm. The permanent magnet consists of a stack of seven NdFeB cubes with a lateral dimension of 5 mm. In this geometry, the magnetic field gradient applied to the free end of the fiber is of the order of 0.1 T m^{-1} [45]. The frames are taken one second apart from Video S1. The magnet is moved from left to right and then left again, thus imparting a joystick-like motion to the fiber. (b) Sequence of images clearly showing the bending response of a 100nm fiber, mounted on a fixed support in cantilever geometry, when the permanent magnet is brought close to the free end (frames taken from Video S2).

the initial phases of the layer growth process [45]. Moreover, it should be considered that in the sputtering process, the flux of impinging atoms decreases with the arrival angle [57]. Therefore, the thickness of the FeCo layer was certainly not uniform, i.e., it was greater in the area of the fiber facing the incoming atoms (arrival angle ∼0°) than on the sides (arrival angle ∼90°). Hence, for each type of fiber, we estimated an effective uniform thickness of the FeCo coating, obviously lower than the nominal one (i.e., ∼1.5, 3.7, and 63 nm, instead of 5nm, 10nm, and 100nm, respectively), and the volume fraction of the magnetic component (Table S1).

The sequence of images in Figure 6 clearly shows that a 100nm fiber, in which the FeCo volume fraction is slightly less than 1%, can be readily actuated by a magnetic field gradient (see also Videos S1 and S2). A weaker, but well-appreciable magnetic bending response was also observed in a 10nm fiber, having a FeCo volume fraction of ∼0.05% (Video S3). Interestingly, the magnetic actuation performance of freshly prepared and aged samples did not undergo appreciable changes. Indeed, Videos S2 and S3 were recorded more than six months after the FeCo layer was deposited on the fibers, a period during which the samples were kept in ambient air. This long-term stability is consistent with the presence of a passivating oxide layer on the FeCo coating of fresh samples, as also indicated by the values of M_S found in the REF films, which are slightly lower than that of the bulk alloy (see Table S1 and related information). To definitely assess this stability, SQUID measurements on the samples of FeCo-coated fibers were repeated after six months of aging in ambient air; the measured magnetic moments, also reported in Table S1, remained aligned to the initial values within the experimental error, confirming the absence of significant degradation.

3.3.2 | Analysis of the Magnetic Hysteretic Behavior

Magnetic hysteresis loops were measured by MOKE magnetometry at room temperature on the FeCo-coated fibers, with the magnetic field applied parallel and perpendicular to the fiber

16163028, 2026, 48, Downloaded from https://advanced.onlinelibrary.wiley.com/doi/10.1002/adfm.75699 by Universita Di Ferrara, Wiley Online Library on [23/06/2026]. See the Terms and Conditions (https://onlinelibrary.wiley.com/terms-and-conditions) on Wiley Online Library for rules of use; OA articles are governed by the applicable Creative Commons License

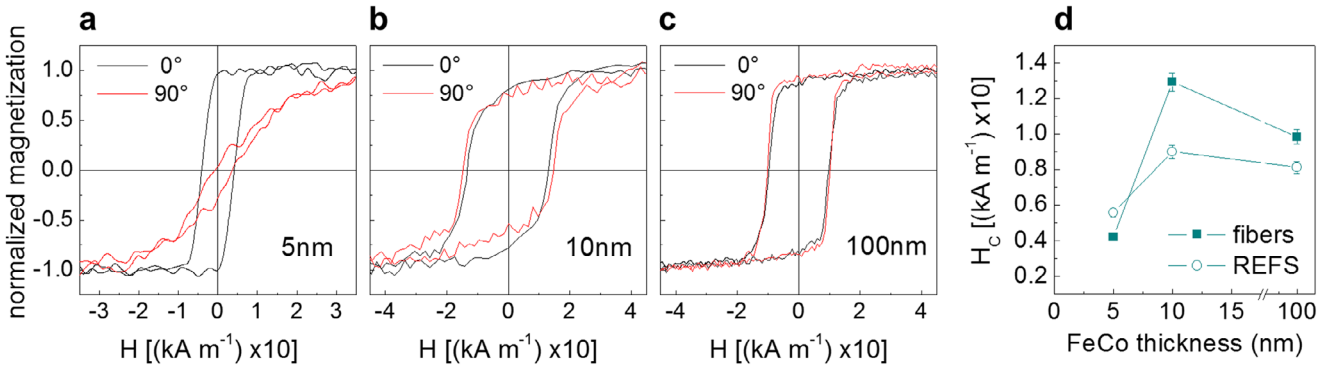

FIGURE 7 | Representative magnetic hysteresis loops measured in the 0° and 90° directions on (a) 5nm, (b) 10nm, and (c) 100nm fibers. (d) Coercivity H_C measured on the coated fibers and on the corresponding REF films, shown as a function of the nominal FeCo layer thickness.

long axis, which we indicate as directions 0° and 90°, respectively (Figure 2c). Typical results are displayed in Figure 7a–c.

The 5nm fiber exhibits a pronounced anisotropic magnetic behavior, as revealed by the different shapes of the loops measured in the 0° and 90° directions, which turn out to be an easy and a hard magnetization axis, respectively. On the contrary, the 10nm and 100nm fibers show isotropic behavior. The normalized remanent magnetization is ∼0.8 in the 10nm fiber and ∼0.9 in the 100nm fiber, i.e., the loops of the latter are more square. Regarding the three REF films, magnetic loops, measured by MOKE on applying the field along two orthogonal in-plane directions, revealed an isotropic behavior, and the normalized remanent magnetization was larger than 0.9 (Figure S5).

In Figure 7d, the values of coercivity H_C measured on the fibers in the 0° direction are reported as a function of the FeCo thickness, together with those of the REF films. In both sets of samples, H_C is minimum at a FeCo thickness of 5nm and maximum at 10nm.

Based on X-ray diffraction analysis (see Figure S6 and related information), both in the REF films and in the fibers the FeCo mean grain size was smaller than the exchange ferromagnetic length of the FeCo alloy (∼20nm) [58, 59]. Therefore, in agreement with the prediction of the random anisotropy model for nanocrystalline materials, the magnetocrystalline anisotropy (MCA) is expected to average out to a vanishingly small value in all the investigated samples [58]. However, it is well known that mechanical stresses develop in the deposited film during the sputtering process and, since the FeCo alloy is magnetostrictive, this event can cause the onset of magnetoelastic anisotropy (MEA) [60–62]. Thus, the presented magnetic results allow the following description to be drawn. The low H_C measured in the thinnest FeCo layer (i.e., 5nm, both fiber and REF film) indicates that, just like the MCA, also the MEA is negligible (Figure 7d). This suggests that short-ranged and randomly oriented built-in stresses develop in this very thin layer, so that MEA averages out to a close to zero value. In this view, the anisotropic hysteretic behavior observed in the 5nm fiber (Figure 7a) may be related to the wrinkled morphology of the polymer substrate, which can determine, in the thin FeCo coating, the onset of a shape anisotropy easy axis directed along the fiber itself. In other words, it appears that in the 5nm fiber, both the MCA and MEA are so weak that shape anisotropy predominates.

In the 10nm fiber, the high H_C value, which is also considerably larger than that of the REF film (Figure 7d), is to be related to the onset of a MEA contribution, revealing the presence of significant long-range built-in stresses (Figure 7b). The shape of the loop, presenting a rather low remanent magnetization, is consistent with a magnetization reversal process mainly governed by motion of walls of already nucleated magnetic domains having different orientations of the magnetization vector. This implies the presence of pinning points for the domain walls, and therefore an irregular and defective microstructure of the FeCo coating. In magnetostrictive materials the displacement of the domain walls is also hindered by internal mechanical stresses [63].

A square hysteresis loop, like that of the REF films (Figure S5), is a signature of a magnetization reversal process dominated by nucleation of large magnetic domains and unimpeded wall motion, and is therefore typically observed in samples with a homogeneous, defect-free microstructure [63]. Accordingly, the square loops measured in the 100nm fiber indicate a more regular microstructure of the FeCo coating (Figure 7c), compared to that in the 10nm fiber. Moreover, the lower value of H_C is consistent with a decrease in MEA (Figure 7d), implying that the presence of built-in stresses tends to reduce in thicker FeCo layers. This is in agreement with the behavior observed in metals like Co and Fe, where the stress induced by the Volmer-Weber growth mechanism slightly decreases as the thickness of the film increases [64, 65]. However, also in the 100nm fiber H_C is larger than that of the corresponding REF film (Figure 7d), indicating that the presence of structural defects and stresses in the coating remains relevant.

It is also to be considered that MOKE magnetometry is essentially a surface technique, as light can penetrate metals to a depth of a few tens of nanometers [66]. Therefore, MOKE collects the magnetic signal from the entire 5nm and 10nm thick FeCo layers, while only the top part of the 100nm thick FeCo layer is probed. Moreover, in each MOKE measurement, only an area corresponding to the focused laser spot is investigated. However, the trend of H_C vs. FeCo thickness shown in Figure 7d was confirmed by measurements performed on fiber samples using

16163028, 2026, 48, Downloaded from https://advanced.onlinelibrary.wiley.com/doi/10.1002/adfm.75699 by Universita Di Ferrara, Wiley Online Library on [23/06/2026]. See the Terms and Conditions (https://onlinelibrary.wiley.com/terms-and-conditions) on Wiley Online Library for rules of use; OA articles are governed by the applicable Creative Commons License

SQUID magnetometry, which is a volume-sensitive technique (Figure S7).

3.4 | Magnetic Study of the FeCo-Coated Fibers Under Mechanical Strain

3.4.1 | Magnetomechanical Coupling and Hysteretic Behavior

Magnetic hysteresis loops were measured by MOKE on the FeCo-coated fibers with H parallel to the long axis (0° direction; Figure 8a) on increasing the distance between the two arms of the sample holder (Figure 2a,b), i.e., varying the mechanical strain ε imparted to the polymer fiber. The shape of the magnetic loops changed on straining the fibers, particularly the coercivity, as shown in Figure 8b. This is to be ascribed to the appearance of MEA anisotropy, whose coefficient is given by the relation $K = (3/2)\lambda_S\sigma$, where λ_S is the saturation magnetostriction and σ is the tensile stress in the FeCo coating. Since λ_S is positive in FeCo ($\sim 6 \times 10^{-5}$), the tensile stress direction, i.e., the fiber long axis, is expected to be an easy magnetization axis [63].

The detection of the magnetomechanical response in the fibers is a noteworthy result that demonstrates the effective adhesion of the FeCo coating to the silk substrate. Figure 8b reveals that the response to the mechanical stimulus, as detected by MOKE, crucially depends on the FeCo thickness.

The highest H_C increment (~250%) is achieved in the 5nm fiber at $\varepsilon = 2\%$; no further increase in H_C is observed at higher strain, but rather it decreases slightly (for $\varepsilon > 6\%$, a drastic reduction in the MOKE signal-to-noise ratio was experienced, and the analysis did not provide reliable results). In the 10nm fiber, the increment in H_C is still remarkable (~200%) and is mainly obtained by increasing the strain up to 8%, while for higher strain values, H_C is the same within the errors. In the 100nm fiber, a significant increase in H_C (~20%) is observed only at $\varepsilon = 14\%$ and it does not change at higher strain. Hence, the strain at which H_C reaches a plateau increases with increasing FeCo thickness.

Figure 8c–e shows representative hysteresis loops measured under strain. In the unstrained 5nm fiber, we already established that the long axis was an easy magnetization axis due to the shape anisotropy (Figure 7a). Therefore, apart from the increase in H_C, the loop shape does not change with the application of the strain (Figure 8c). On the contrary, in the 10nm fiber, an improvement of the loop squareness is clearly observed (Figure 8d). This reveals that, upon the strain application, the originated MEA becomes the predominant anisotropy contribution. A similar effect is observed also in the 100nm fiber (Figure 8e), but it is much weaker since the loop at $\varepsilon = 0\%$ is already rather square (as commented in Section 3.3.2).

SEM analysis was performed on the fibers previously characterized by MOKE (Figure 8b) to correlate the magnetic response with the morphological evolution of the coating. Figure 8f is a representative image of the 5nm fiber, where the non-uniform contrast—characterized by alternating dark and light gray areas—is consistent with a FeCo coating broken into small fragments that partially detached from the fiber and most likely curled up.

A different morphology characterizes wide areas of the 10nm fiber (Figure 8g). Here, large cracks coexist with bright wrinkles oriented perpendicular to the fiber's long axis. These features correspond to regions where the FeCo coating has thickened, likely due to the following mechanism: the metal layer undergoes fracture under the applied strain; once the strain is removed, the polymer fiber recovers its original length more effectively than the metallic fragments. Consequently, the fragments are pushed against each other, leading to the observed wrinkling effect. Thus, the distance between these bright features can be taken as an estimate of the fragment size. In the 100nm fiber, the coating appears partitioned into significantly larger, roughly rectangular pieces (Figure 8h).

Notably, this analysis reveals a correlation between coating thickness and fragment dimensions: thicker coatings result in larger islands, ranging from the sub-micrometric scale in the 5nm fiber to approximately 10 μm in the 100nm fiber. Despite the fragmentation observed in all three samples, the FeCo pieces remain sufficiently attached to the polymer fiber to allow for the detection of the MOKE signal (Figure 8b).

Taken together, the magnetic characterization and the morphological analysis allow a comprehensive picture of the magnetomechanical response in the fibers to be drawn.

The thickness-dependence of H_C under strain (Figure 8b) can be interpreted through the lens of the shear-lag model, which describes the transfer of load from a compliant substrate to a stiffer overlayer through interfacial shear stresses, resulting in a non-uniform buildup of tensile stress within the coating [67–69]. The model predicts that the internal stress buildup depends on the ratio between the silk/FeCo interfacial area and the metallic volume and hence scales inversely with the coating thickness. In the 5nm fiber, this ratio is maximized. This results in a steep buildup of internal stress throughout the FeCo layer, even at low applied strain, triggering the observed increment of H_C. In the thicker coatings of the 10nm and 100nm fibers, the transferred stress is distributed through a much larger volume. Therefore, the average internal stress is significantly lower than in the thinner coating, explaining the lower H_C increment measured in these samples. In this mechanism, a crucial role is played by the strong mechanical contrast between the polymer and the metallic layer (i.e., the deposited phase is much stiffer than the substrate) [70, 71]. In the case of the 100nm fiber, the weak H_C variation even at high strain may also be a consequence of the surface-sensitive nature of the MOKE technique, which implies that we collected the magnetic signal coming from the top of the FeCo coating, where the effective strain is minimized (performing SQUID measurements on strained fibers to complement MOKE analysis is not feasible).

This description, however, is not complete, as it needs to be refined considering that the accumulation of internal stress is

16163028, 2026, 48, Downloaded from https://advanced.onlinelibrary.wiley.com/doi/10.1002/adfm.75699 by Universita Di Ferrara, Wiley Online Library on [23/06/2026]. See the Terms and Conditions (https://onlinelibrary.wiley.com/terms-and-conditions) on Wiley Online Library for rules of use; OA articles are governed by the applicable Creative Commons License

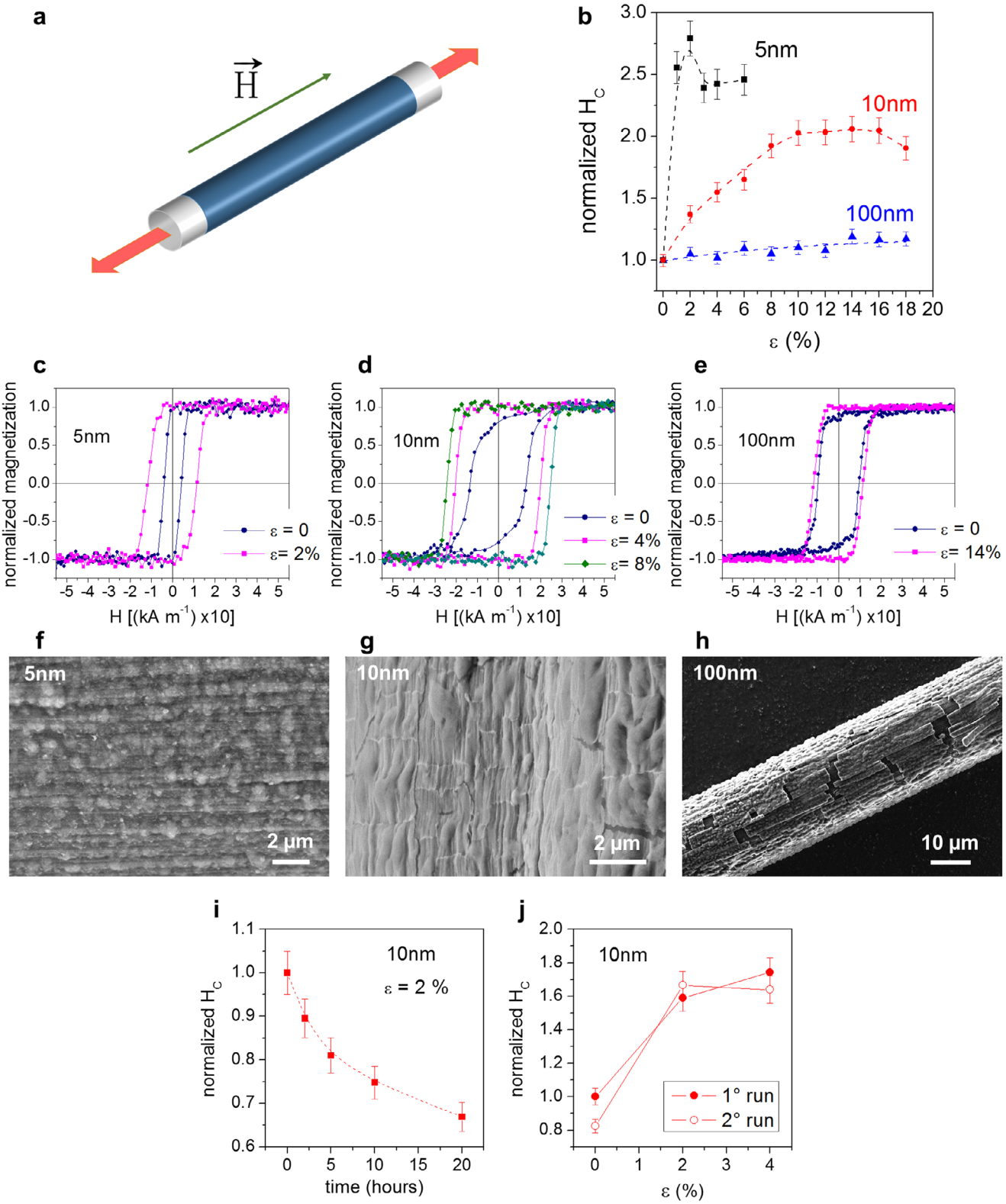

FIGURE 8 | (a) Scheme showing the FeCo-coated fiber stretched at the ends and the direction of the magnetic field (0° direction) during the analysis of the magnetomechanical response by MOKE. (b) Coercivity H_C as a function of the strain ε imparted to the fibers (the H_C values are normalized to that at zero strain); the dotted lines are guides to the eye. (c–e) Representative magnetic hysteresis loops measured at the indicated values of ε. (f–h) SEM secondary electrons images of the fibers after being subjected to the measurements reported in frame (b) (the image in f was taken in variable-pressure mode). (i) Evolution with time of H_C, measured on a 10nm fiber kept at a strain $\varepsilon = 2\%$ (the curve is normalized to its initial value; the dotted line is a guide to the eye). (j) Curves of H_C vs. ε, corresponding to two consecutive runs of measurements on a 10nm fiber (the H_C values are normalized to those measured at zero strain in the first run).

16163028, 2026, 48, Downloaded from https://advanced.onlinelibrary.wiley.com/doi/10.1002/adfm.75699 by Universita Di Ferrara, Wiley Online Library on [23/06/2026]. See the Terms and Conditions (https://onlinelibrary.wiley.com/terms-and-conditions) on Wiley Online Library for rules of use; OA articles are governed by the applicable Creative Commons License

not indefinite but is governed by the fragmentation process. The inherent roughness and the presence of pre-existing cracks in the coating (Figure 3) act as nucleation sites that, as the fiber is stretched, facilitate the evolution into a stable fragmented morphology.

According to the shear-lag model, the internal tensile stress in a fragment is zero at its edges and increases toward the center [68]. This buildup requires a characteristic transfer length to reach its maximum value; therefore, the maximum stress that can be transferred to a fragment is strictly dependent on its length-to-thickness ratio. The terminal fragmentation regime sets in when fragments become, on average, too short to sustain further stress buildup up to their breaking point, regardless of additional substrate elongation. At this point, H_C stops increasing, leading to the observed plateau (Figure 8b). This framework is consistent with the morphologies observed via SEM (Figure 8f–h), which show that thicker coatings break into larger fragments [68, 72]. As the coating thickness increases, a significantly higher applied strain is required to transfer sufficient stress to sustain continuous fragmentation until stress saturation is reached. Specifically, the 5nm fiber reaches the H_C plateau at a low strain ($\varepsilon \sim 2\%$). In contrast, stress saturation is shifted to higher strain levels for the 10nm ($\varepsilon \sim 8\%$) and 100nm fibers ($\varepsilon \sim 14\%$). Ultimately, the shift of the H_C plateau toward higher strain values in thicker coatings reflects the greater mechanical work required to drive the fragmentation of the thicker metallic layer until the terminal regime is reached.

Indeed, the continuous increase of H_C up to the plateau value serves as a direct experimental validation of the effective interfacial adhesion between the silk fiber and the FeCo coating and provides an indirect measure of the interfacial shear strength. In fact, the internal stress in the coating can only increase as long as the interface sustains the shear stress necessary to transfer the load from the strained fiber. The fact that the magnetoelastic response tracks the deformation up to strain values far beyond the yield point of metals (i.e., $\varepsilon < 1\%$ [73, 74]) proves that the interface is mechanically robust and capable of efficient stress transfer. This indicates that the critical shear strength of the silk/FeCo interface is high enough to allow the fragments to reach their terminal size before any significant delamination or interfacial sliding occurs, as also confirmed by the SEM analysis of the 10nm and 100nm fibers (Figure 8g,h). Therefore, reaching the H_C plateau does not imply a loss of adhesion, but rather signals that the physical limit of stress transfer for that specific fragment morphology has been attained. Indeed, the 5nm fiber represents an exception: here, the terminal fragment size is so small that, once the H_C plateau is reached, a secondary stress-relief mechanism takes over. In fact, the fragmentation into sub-micrometric islands is followed by their curling (Figure 8f). This indicates that while the interfacial adhesion is efficient enough to drive the fragmentation to its physical limit at low strain, it is insufficient to preserve the planar configuration of such ultra-thin islands. This loss of planarity leads to significant light scattering, providing a physical rationale for the drastic reduction in the MOKE signal-to-noise ratio observed in the 5nm fiber at $\varepsilon > 6\%$, which ultimately prevented reliable H_C measurements in this regime (Figure 8b).

3.4.2 | Time Evolution of the Magnetomechanical Response

The magnetomechanical response of the FeCo-coated fibers showed a remarkable time dependence, which we monitored by analyzing the temporal evolution of H_C on a 10nm fiber kept at a strain $\varepsilon = 2\%$. We focused on this type of fiber because it had the highest H_C in both the unstrained and strained state (Figures 7b and 8d), making any variations clearly discernible. Figure 8i shows that H_C decreases by approximately 35% within 20 h, which is to be attributed to stress relaxation within the magnetic coating over time. It is to be noted that the mechanical tests reported in Figure 5 indicated that both the as-prepared fiber and the coated ones exhibited stress relaxation on a time scale of the order of minutes. It is worth remarking that while mechanical tests probed the whole fiber, the MOKE analysis probed the magnetic coating exclusively. Therefore, the relaxation phenomenon displayed in Figure 8i can be explained by considering that the applied strain promotes the growth kinetics of both the existing cracks in the as-sputtered FeCo coating (Figure 3b) and of newly formed cracks.

This results in a progressive release of the stress transferred from the substrate and built-in stresses in the coating, leading to a gradual reduction of the mechanical energy stored in the FeCo layer as the crack network slowly evolves.

In Figure 8j two curves of H_C vs. ε are reported, corresponding to two consecutive runs of measurements on a 10nm fiber. The coercivity at zero strain in the second run, recorded approximately 2 h after the start of the experiment, is significantly lower than that measured in the first run. This confirms that relaxation of built-in stresses occurred in the FeCo coating during the first run. Interestingly, the values of H_C measured at higher strain, up to $\varepsilon = 4\%$, in the two runs are similar within the errors, namely the macroscopic magnetomechanical response appears to be reversible. This reversibility indicates that, after the initial relief of built-in stresses during the first run, the magnetomechanical response is dominated by the elastic transfer of stress to a stable population of fragments, rather than the nucleation of new fractures. We focused on the 0%–4% strain range as it represents the most dynamic part of the H_C vs. ε curve, where the coercivity shows the steepest increase (Figure 8b). For higher strain, particularly approaching the H_C plateau at $\varepsilon \sim 8\%$, the MOKE signal-to-noise ratio degrades, preventing reliable data acquisition during the second measurement run. This is to be ascribed to the increased density of fractures at higher strain, which promotes diffuse scattering at the expense of the specular reflection required for a reliable MOKE signal.

4 | Conclusions

We demonstrated the potential of a new pathway for producing artificial spider silk fibers with magnetic and magnetomechanical responsiveness, which consists in coating them with a thin layer of ferromagnetic and magnetostrictive FeCo alloy by sputtering deposition. We reported that composite fibers with a volume fraction of FeCo less than 1% were readily activated by a magnetic field gradient and that such a small metal fraction was sufficient

16163028, 2026, 48, Downloaded from https://advanced.onlinelibrary.wiley.com/doi/10.1002/adfm.75699 by Universita Di Ferrara, Wiley Online Library on [23/06/2026]. See the Terms and Conditions (https://onlinelibrary.wiley.com/terms-and-conditions) on Wiley Online Library for rules of use; OA articles are governed by the applicable Creative Commons License

to make them electrically conductive. In short, we pinpointed a very promising strategy for the development of biopolymer-based composite materials with enhanced functionalities. However, achieving this goal could not be separated from the need to better understand how the mutual influence between the protein-based fiber and the metal coating determined the mechanical and magnetic properties of the composite material. This was a primary aim of our work, and the analysis of fibers with FeCo coating of different nominal thickness (5nm, 10nm, and 100nm) provided valuable insights in this regard, which are summarized here.

1. The mechanical properties of the FeCo-coated fibers were satisfactorily close to those of the as-prepared material, especially with regard to strength and Young's modulus. A significant decrease of 30%–40% in ductility and toughness was observed only in the 100nm fiber. Mechanical tests indicated that both the as-prepared and coated fibers underwent viscoelastic stress relaxation on a time scale of the order of minutes.
2. The FeCo coating had an effective thickness lower than the nominal one, which is attributable to the peculiar nature and geometry of the substrate (i.e., the polymer fiber), compared to traditional substrates (e.g., the Si one used for the REF films). Moreover, the FeCo coating morphology was strongly determined by that of the underlying fiber and was also characterized by the presence of cracks and built-in stresses. All of this had an impact on the type of dominant magnetic anisotropy and hence on the hysteretic behavior of the fibers, which ultimately turned out to be related to the FeCo thickness.
3. The detection of a significant magnetomechanical response confirmed the excellent adhesion of the FeCo layer to the polymer substrate. The H_C increment—which in the 5nm fiber reached ~250% at $\varepsilon = 2\%$—decreased with increasing the FeCo thickness, indicating that, in accordance with the shear-lag model, this parameter governs the stress transmission from the fiber to the coating. The observed plateau in the H_C vs. ε curves marks the attainment of a terminal fragmentation regime, where the fragments become, on average, too short to allow further effective stress buildup.
4. The evolution of the magnetomechanical response over time was correlated with the release of mechanical energy in the coating, driven by the slow propagation kinetics of pre-existing and newly formed cracks. This process occurred on a much longer time scale than the stress relaxation in whole fibers (hours vs. minutes), indicating that the two phenomena are governed by different physical mechanisms. Notably, after the initial relief of built-in stresses, the magnetomechanical response was found to be reversible up to $\varepsilon = 4\%$, being dominated by the elastic transfer of stress to a stable population of fragments.

We believe these findings represent useful guidelines for addressing the challenge of combining organic materials and inorganic magnetic nanostructures and thus taking a step forward towards the creation of bioinspired, robust, and flexible protein-based magnetic fibers.

Author Contributions

Filippo Lanaro: conceptualization, formal analysis, investigation, methodology, validation, visualization, writing- review & editing. Federico Spizzo: conceptualization, formal analysis, investigation, methodology, resources, supervision, validation, visualization, writing-review & editing. Gabriele Greco: conceptualization, formal analysis, funding acquisition, investigation, methodology, validation, visualization, writing- review & editing. Benjamin Schmuck: investigation, validation, writing- review & editing. Anna Rising: resources, supervision, writing-review & editing. Lucia Del Bianco: conceptualization, formal analysis, funding acquisition, methodology, resources, supervision, visualization, writing the original draft, writing- review & editing.

Acknowledgements

The research work of L.D.B. was supported by the University of Ferrara under projects FIRD-2024 and FIRD-2025. The authors acknowledge the use of the instruments at the Electron Microscopy Center of the University of Ferrara and the scientific and technical assistance of Negar Eftekhari and Cinzia Brenna. G.G. was supported by the project "EPASS" under the HORIZON TMA MSCA Postdoctoral Fellowships—European Fellowships (project number 101103616). B.S. was supported by FORMAS (2023-00871). A.R. is supported by Olle Engkvist stiftelse (233-0334), Knut and Alice Wallenberg Foundation (2023.0331), European Research Council (ERC) under the European Union's Horizon 2020 research and innovation program (grant agreements No. 1010693 ArtSilkTex and No 815357 ARTSILK), FORMAS (2023-01313), and the Swedish Research Council (2024-02919).

Open access publishing facilitated by Universita degli Studi di Ferrara, as part of the Wiley - CRUI-CARE agreement.

Conflicts of Interest

The authors declare no conflicts of interest.

Data Availability Statement

The data that support the findings of this study are available from the corresponding authors upon reasonable request.

References

1. S. H. Mir, L. A. Nagahara, T. Thundat, P. Mokarian-Tabari, H. Furukawa, and A. Khosla, "Review—Organic-Inorganic Hybrid Functional Materials: an Integrated Platform for Applied Technologies," *Journal of The Electrochemical Society* 165, no. 8 (2018): B3137–B3156, https://doi.org/10.1149/2.0191808jes.

2. L. Zhang, X. Huang, L. Liu, et al., "Fabrication of Organic/Inorganic Nanocomposites: from Traditional Synthesis to Additive Manufacturing," *Advanced Materials* 37, no. 37 (2025): 2505504, https://doi.org/10.1002/adma.202505504.

3. B. Liu, A. S. Desai, X. Sun, et al., "An Overview of Sustainable Biopolymer Composites in Sensor Manufacturing and Smart Cities," *Advanced Composites and Hybrid Materials* 7, no. 5 (2024): 146, https://doi.org/10.1007/s42114-024-00938-y.

4. S. Deb, in *Advanced Bionanocomposite Materials: Innovations for Sustainable Development*, edited by S. C. George and B Tawiah (Springer Nature, 2025), 397, https://doi.org/10.1007/978-981-96-8225-6_11.

5. M. Saranya, V. P. Krithika, and D. Senthamilselvi, *Green Chemistry Methods for Producing Biopolymeric Nanomaterials* (Springer Nature, 2025), 161, https://doi.org/10.1007/978-981-96-9501-0_6.

6. R. N. Darie-Niță and S. Frąckowiak, "An Overview of Potential Applications of Environmentally Friendly Hybrid Polymeric Materials," *Polymers* 17, no. 2 (2025): 252, https://doi.org/10.3390/polym17020252.

16163028, 2026, 48, Downloaded from https://advanced.onlinelibrary.wiley.com/doi/10.1002/adfm.75699 by Universita Di Ferrara, Wiley Online Library on [23/06/2026]. See the Terms and Conditions (https://onlinelibrary.wiley.com/terms-and-conditions) on Wiley Online Library for rules of use; OA articles are governed by the applicable Creative Commons License

7. A. Garcia, C. R. Tubio, R. Seoane-Rivero, L. Rubio-Peña, and S. Lanceros-Mendez, "Magnetoactive and Electroactive Biobased and Biopolymer Composites," *Sustainable Materials & Technologies* 45 (2025): e01485, https://doi.org/10.1016/j.susmat.2025.e01485.

8. E. Yarali, M. Baniasadi, A. Zolfagharian, et al., "Magneto-/ Electro-Responsive Polymers toward Manufacturing, Characterization, and Biomedical/Soft Robotic Applications," *Applied Materials Today* 26 (2022): 101306, https://doi.org/10.1016/j.apmt.2021.101306.

9. S. Wu, W. Hu, Q. Ze, M. Sitti, and R. Zhao, "Multifunctional Magnetic Soft Composites: A Review," *Multifunctional Materials* 3, no. 4 (2020): 042003, https://doi.org/10.1088/2399-7532/abcb0c.

10. M. Du, S. Lv, J. Qiu, T. Guo, and S. Zhou, "Multimaterial Fibers for Multifunctional Sensing Applications," *Laser & Photonics Reviews* 18, no. 10 (2024): 2301125, https://doi.org/10.1002/lpor.202301125.

11. A. Kiseleva, G. Kiselev, V. Kessler, et al., "Optically Active Hybrid Materials Based on Natural Spider Silk," *ACS Applied Materials & Interfaces* 11, no. 26 (2019): 22962–22972, https://doi.org/10.1021/acsami.9b05131.

12. K. K. Ahmed, D. Q. Muheddin, P. A. Mohammed, et al., "A Brief Review on Optical Properties of Polymer Composites: Insights into Light-Matter Interaction from Classical to Quantum Transport Point of View," *Results in Physics* 56 (2024): 107239, https://doi.org/10.1016/j.rinp.2023.107239.

13. X. Xu, Q. Yang, Y. Wang, H. Yu, X. Chen, and X. Jing, "Biodegradable Electrospun Poly(l-lactide) Fibers Containing Antibacterial Silver Nanoparticles," *European Polymer Journal* 42, no. 9 (2006): 2081–2087, https://doi.org/10.1016/j.eurpolymj.2006.03.032.

14. R. Gobi, P. Ravichandiran, R. S. Babu, and D. J. Yoo, "Biopolymer and Synthetic Polymer-Based Nanocomposites in Wound Dressing Applications: A Review," *Polymers* 13, no. 12 (2021): 1962, https://doi.org/10.3390/polym13121962.

15. L. Eisoldt, A. Smith, and T. Scheibel, "Decoding the Secrets of Spider Silk," *Materials Today* 14, no. 3 (2011): 80–86, https://doi.org/10.1016/S1369-7021(11)70057-8.

16. G. Greco, B. Schmuck, S. K. Jalali, N. M. Pugno, and A. Rising, "Influence of Experimental Methods on the Mechanical Properties of Silk Fibers: A Systematic Literature Review and Future Road Map," *Biophysics Reviews* 4, no. 3 (2023): 031301, https://doi.org/10.1063/5.0155552.

17. M. Andersson, J. Johansson, and A. Rising, "Silk Spinning in Silkworms and Spiders," *International Journal of Molecular Sciences* 17, no. 8 (2016): 1290, https://doi.org/10.3390/ijms17081290.

18. A. P. Kiseleva, P. V. Krivoshapkin, and E. F. Krivoshapkina, "Recent Advances in Development of Functional Spider Silk-Based Hybrid Materials," *Frontiers in Chemistry* 8 (2020): 554, https://doi.org/10.3389/fchem.2020.00554.

19. T. Braxton, C. Holland, and G. Greco, "The Circular Argument behind Spider and Silkworm Silk Mechanical Properties," *Materials & Design* 260 (2025): 115224, https://doi.org/10.1016/j.matdes.2025.115224.

20. Y. Kim and X. Zhao, "Magnetic Soft Materials and Robots," *Chemical Reviews* 122, no. 5 (2022): 5317–5364, https://doi.org/10.1021/acs.chemrev.1c00481.

21. Y. Lee, F. Koehler, T. Dillon, et al., "Magnetically Actuated Fiber-Based Soft Robots," *Advanced Materials* 35, no. 38 (2023): 2301916, https://doi.org/10.1002/adma.202301916.

22. N. Ebrahimi, C. Bi, D. J. Cappelleri, et al., "Magnetic Actuation Methods in Bio/Soft Robotics," *Advanced Functional Materials* 31, no. 11 (2021): 2005137, https://doi.org/10.1002/adfm.202005137.

23. D. V. Kladko and V. V. V. Magnetosurgery, "Principles, Design, and Applications," *Smart Materials in Medicine* 5, no. 1 (2024): 24–35, https://doi.org/10.1016/j.smaim.2023.06.008.

24. B. Calmé, A. Metcalf, M. Brockdorff, et al., "Hybrid Tendon-actuated and Soft Magnetic Robotic Platform for Pancreatic Applications," *IEEE Robotics & Automation Letters* 10, no. 2 (2025): 1784–1791, https://doi.org/10.1109/LRA.2024.3524889.

25. H. Banerjee, A. Leber, S. Laperrousaz, et al., "Soft Multimaterial Magnetic Fibers and Textiles," *Advanced Materials* 35, no. 33 (2023): 2212202, https://doi.org/10.1002/adma.202212202.

26. E. Xue, L. Liu, W. Wu, and B. Wang, "Soft Fiber/Textile Actuators: from Design Strategies to Diverse Applications," *ACS Nano* 18, no. 1 (2024): 89–118, https://doi.org/10.1021/acsnano.3c09307.

27. T. Schiller and T. Scheibel, "Bioinspired and Biomimetic Protein-based Fibers and Their Applications," *Communications Materials* 5, no. 1 (2024): 56, https://doi.org/10.1038/s43246-024-00488-2.

28. E. L. Mayes, F. Vollrath, and S. Mann, "Fabrication of Magnetic Spider Silk and Other Silk-Fiber Composites Using Inorganic Nanoparticles," *Advanced Materials* 10, no. 10 (1998): 801–805, https://doi.org/10.1002/(SICI)1521-4095(199807)10.

29. A. Kryuchkova, M. Mikhailova, P. Zelenovskii, et al., "Nanohybrid Fibers via Direct Nanoparticle Injection into the Spider's Silk Gland," *ACS Applied Bio Materials* 8, no. 7 (2025): 6145–6158, https://doi.org/10.1021/acsabm.5c00680.

30. F. Spizzo, G. Greco, L. Del Bianco, M. Coïsson, and N. M. Pugno, "Magnetostrictive and Electroconductive Stress-Sensitive Functional Spider Silk," *Advanced Functional Materials* 32, no. 44 (2022): 2207382, https://doi.org/10.1002/adfm.202207382.

31. M. Jani, M. Ramírez, and J. O. Wolff, "Methods to Identify Silk Gland Activation Patterns in Spider Spinning Behaviors," *The Journal of Arachnology* 53, no. 2 (2025): 125–133, https://doi.org/10.1636/joa-s-24-016.

32. D. R. Whittall, K. V. Baker, R. Breitling, and E. Takano, "Host Systems for the Production of Recombinant Spider Silk," *Trends in Biotechnology* 39, no. 6 (2021): 560–573, https://doi.org/10.1016/j.tibtech.2020.09.007.

33. M. Michel and T. Scheibel, "Fiber Processing of Recombinant Spider Silk Proteins," *Journal of Polymer Science* 63, no. 21 (2025): 4573–4586, https://doi.org/10.1002/pol.20250083.

34. A. Heidebrecht, L. Eisoldt, J. Diehl, et al., "Biomimetic Fibers Made of Recombinant Spidroins with the Same Toughness as Natural Spider Silk," *Advanced Materials* 27, no. 13 (2015): 2189–2194, https://doi.org/10.1002/adma.201404234.

35. T. Arndt, G. Greco, B. Schmuck, et al., "Engineered Spider Silk Proteins for Biomimetic Spinning of Fibers with Toughness Equal to Dragline Silks," *Advanced Functional Materials* 32, no. 23 (2022): 2200986, https://doi.org/10.1002/adfm.202200986.

36. B. Schmuck, G. Greco, T. B. Pessatti, et al., "Strategies for Making High-Performance Artificial Spider Silk Fibers," *Advanced Functional Materials* 34, no. 35 (2024): 2305040, https://doi.org/10.1002/adfm.202305040.

37. B. Schmuck, G. Greco, F. G. Bäcklund, N. M. Pugno, J. Johansson, and A. Rising, "Impact of Physio-Chemical Spinning Conditions on the Mechanical Properties of Biomimetic Spider Silk Fibers," *Communications Materials* 3, no. 1 (2022): 83, https://doi.org/10.1038/s43246-022-00307-6.

38. M. Andersson, Q. Jia, A. Abella, et al., "Biomimetic Spinning of Artificial Spider Silk from a Chimeric Minispidroin," *Nature Chemical Biology* 13, no. 3 (2017): 262–264, https://doi.org/10.1038/nchembio.2269.

39. B. Schmuck, G. Greco, A. Barth, N. M. Pugno, J. Johansson, and A. Rising, "High-Yield Production of a Super-Soluble Miniature Spidroin for Biomimetic High-Performance Materials," *Materials Today* 50 (2021): 16–23, https://doi.org/10.1016/j.mattod.2021.07.020.

40. G. Greco, B. Schmuck, L. Del Bianco, et al., "High-Performance Magnetic Artificial Silk Fibers Produced by a Scalable and Eco-Friendly Production Method," *Advanced Composites and Hybrid Materials* 7, no. 5 (2024): 163, https://doi.org/10.1007/s42114-024-00962-y.

41. L. Del Bianco, B. Schmuck, F. Spizzo, et al., "Artificial Spider Silk Fibers with Embedded Magnetite Nanoparticles," *Macromolecular*

16163028, 2026, 48, Downloaded from https://advanced.onlinelibrary.wiley.com/doi/10.1002/adfm.75699 by Universita Di Ferrara, Wiley Online Library on [23/06/2026]. See the Terms and Conditions (https://onlinelibrary.wiley.com/terms-and-conditions) on Wiley Online Library for rules of use; OA articles are governed by the applicable Creative Commons License

Materials and Engineering 310, no. 11 (2025): 00249, https://doi.org/10.1002/mame.202500249.

42. J. L. Dormann, D. Fiorani, and E. Tronc, "Magnetic Relaxation in Fine-Particle Systems," *Advances in Chemical Physics* 98 (1997): 283, https://doi.org/10.1002/9780470141571.ch4.

43. L. Del Bianco, F. Spizzo, G. Barucca, et al., "Mechanism of Magnetic Heating in Mn-Doped Magnetite Nanoparticles and the Role of Intertwined Structural and Magnetic Properties," *Nanoscale* 11, no. 22 (2019): 10896–10910, https://doi.org/10.1039/c9nr03131f.

44. M. Coduri, P. Masala, B. L. Del, et al., "Local Structure and Magnetism of Fe_2O_3 Maghemite Nanocrystals: the Role of Crystal Dimension," *Nanomaterials* 10, no. 5 (2020): 867, https://doi.org/10.3390/nano10050867.

45. L. Del Bianco, F. Spizzo, F. Lanaro, et al., "Silk Fibroin Film Decorated with Ultralow FeCo Content by Sputtering Deposition Results in a Flexible and Robust Biomaterial for Magnetic Actuation," *ACS Applied Materials & Interfaces* 16, no. 38 (2024): 51364–51375, https://doi.org/10.1021/acsami.4c12853.

46. J. A. Rogers, T. Someya, and Y. Huang, "Materials and Mechanics for Stretchable Electronics," *Science* 327, no. 5973 (2010): 1603–1607, https://doi.org/10.1126/science.1182383.

47. "Electronics Can be More Sustainable," *Nature Materials* 22, no. 11 (2023) 1273, https://doi.org/10.1038/s41563-023-01731-w.

48. J. M. D. Coey, *Magnetism and Magnetic Materials* (Cambridge University Press, 2012), https://doi.org/10.1017/CBO9780511845000.

49. R. S. Sundar and S. C. Deevi, "Soft Magnetic FeCo Alloys: Alloy Development, Processing, and Properties," *International Materials Reviews* 50, no. 3 (2005): 157–192, https://doi.org/10.1179/174328005×14339.

50. C. A. Schneider, W. S. Rasband, and K. W. Eliceiri, "NIH Image to ImageJ: 25 Years of Image Analysis," *Nature Methods* 9, no. 7 (2012): 671–675, https://doi.org/10.1038/nmeth.2089.

51. P. Vavassori, "Polarization Modulation Technique for Magneto-optical Quantitative Vector Magnetometry," *Applied Physics Letters* 77, no. 11 (2000): 1605–1607, https://doi.org/10.1063/1.1310169.

52. Z. Q. Qiu and S. D. Bader, "Surface Magneto-Optic Kerr Effect," *Review of Scientific Instruments* 71, no. 3 (2000): 1243–1255, https://doi.org/10.1063/1.1150496.

53. G. Greco, B. Schmuck, F. G. Bäcklund, G. Reiter, and A. Rising, "Post-Spin Stretch Improves Mechanical Properties, Reduces Necking, and Reverts Effects of Aging in Biomimetic Artificial Spider Silk Fibers," *ACS Applied Polymer Materials* 6, no. 23 (2024): 14342–14350, https://doi.org/10.1021/acsapm.4c02192.

54. R. Ene, C. Krywka, S. G. Kang, et al., "Structure Changes in Nephila Dragline: the Influence of Pressure," *Polymer* 53, no. 24 (2012): 5507–5512, https://doi.org/10.1016/j.polymer.2012.09.045.

55. F. Faupel, V. Zaporojtchenko, and T. Strunskus, "Fundamental Aspects of Polymer Metallization," in *Metallization of Polymers*, edited by E. Sacher, (Springer, 2002), p. 73, https://doi.org/10.1007/978-1-4615-0563-1_8.

56. A. Thran, M. Kiene, V. Zaporojtchenko, and F. Faupel, "Condensation Coefficients of ag on Polymers," *Physical Review Letters* 82, no. 9 (1999): 1903–1906, https://doi.org/10.1103/PhysRevLett.82.1903.

57. J. Cook, "Angular Distribution of Sputtered Atoms in Physical Vapor Deposition and Collimated Sputtering," *Thin Solid Films* 338, no. 1–2 (1999): 81–87, https://doi.org/10.1016/S0040-6090(98)01001-3.

58. G. Herzer, "Modern Soft Magnets: Amorphous and Nanocrystalline Materials," *Acta Materialia* 61, no. 3 (2013): 718–734, https://doi.org/10.1016/j.actamat.2012.10.040.

59. M. Vopsaroiu, M. Georgieva, P. J. Grundy, et al., "Preparation of High Moment CoFe Films with Controlled Grain Size and Coercivity," *Journal of Applied Physics* 97, no. 10 (2005): 10N303, https://doi.org/10.1063/1.1855276.

60. G. Abadias, E. Chason, J. Keckes, et al., "Review Article: Stress in Thin Films and Coatings: Current Status, Challenges, and Prospects," *Journal of Vacuum Science & Technology A: Vacuum, Surfaces, and Films* 36, no. 2 (2018): 020801, https://doi.org/10.1116/1.5011790.

61. E. Chason and P. R. Guduru, "Tutorial: Understanding Residual Stress in Polycrystalline Thin Films Through Real-Time Measurements and Physical Models," *Journal of Applied Physics* 119, no. 19 (2016): 191101, https://doi.org/10.1063/1.4949263.

62. F. Spizzo, L. Del Bianco, M. Coïsson, et al., "Interplay between Magnetic Anisotropies in CoAu and Co Films and Antidot Arrays: Effects on the Spin Configuration and Hysteretic Behavior," *Physical Chemistry Chemical Physics* 20, no. 24 (2018): 16835–16846, https://doi.org/10.1039/c8cp02323a.

63. B. D. Cullity and C. D. Graham, *Introduction to Magnetic Materials*, 2nd ed. (Wiley, 2009), https://doi.org/10.1002/9780470386323.

64. G. Abadias, A. Fillon, J. J. Colin, A. Michel, and C. Jaouen, "Real-Time Stress Evolution During Early Growth Stages of Sputter-Deposited Metal Films: Influence of Adatom Mobility," *Vacuum* 100 (2014): 36–40, https://doi.org/10.1016/j.vacuum.2013.07.041.

65. M. Pletea, W. Brückner, H. Wendrock, R. Kaltofen, and R. Koch, "In Situ Stress Evolution of Co Films Sputtered onto Oxidized Si (100) Substrates," *Journal of Applied Physics* 99, no. 3 (2006): 033509, https://doi.org/10.1063/1.2168243.

66. Z. Q. Qiu and S. D. Bader, "Surface Magneto-Optic Kerr Effect (SMOKE)," *Journal of Magnetism and Magnetic Materials* 200, no. 1–3 (1999): 664–678, https://doi.org/10.1016/S0304-8853(99)00311-X.

67. H. L. Cox, "The Elasticity and Strength of Paper and Other Fibrous Materials," *British Journal of Applied Physics* 3, no. 3 (1952): 72–79, https://doi.org/10.1088/0508-3443/3/3/302.

68. A. Kelly and W. R. Tyson, "Tensile Properties of Fibre-Reinforced Metals: Copper/Tungsten and Copper/Molybdenum," *Journal of the Mechanics and Physics of Solids* 13, no. 6 (1965): 329–350, https://doi.org/10.1016/0022-5096(65)90035-9.

69. U. A. Handge, "Analysis of a Shear-Lag Model with Nonlinear Elastic Stress Transfer for Sequential Cracking of Polymer Coatings," *Journal of Materials Science* 37, no. 22 (2002): 4775–4782, https://doi.org/10.1023/A:1020814314019.

70. N. Challab, F. Zighem, D. Faurie, et al., "Local Stiffness Effect on Ferromagnetic Response of Nanostructure Arrays in Stretchable Systems," *Physica Status Solidi (RRL)—Rapid Research Letters* 13, no. 2 (2019): 1800509, https://doi.org/10.1002/pssr.201800509.

71. N. Challab, A. D. Aboumassound, F. Zighem, D. Faurie, and M. Haboussi, "Micromagnetic Modeling of Nanostructures Subject to Heterogeneous Strain Fields," *Journal of Physics D: Applied Physics* 52, no. 35 (2019): 355004, https://doi.org/10.1088/1361-6463/ab229a.

72. Y. Leterrier, J. Andersons, Y. Pitton, and J. A. E. Månson, "Adhesion of Silicon Oxide Layers on Poly (Ethylene Terephthalate). II: Effect of Coating Thickness on Adhesive and Cohesive Strengths," *Journal of Polymer Science Part B: Polymer Physics* 35, no. 9 (1997): 1463–1472, https://doi.org/10.1002/(SICI)1099-0488(19970715)35.

73. S. Tu, X. Ren, J. He, and Z. Zhang, "Stress–Strain Curves of Metallic Materials and Post-Necking Strain Hardening Characterization: a Review," *Fatigue & Fracture of Engineering Materials & Structures* 43, no. 1 (2020): 3–19, https://doi.org/10.1111/ffe.13134.

74. B. Jiang and G. J. Weng, "A Generalized Self-Consistent Polycrystal Model for the Yield Strength of Nanocrystalline Materials," *Journal of the Mechanics and Physics of Solids* 52, no. 5 (2004): 1125–1149, https://doi.org/10.1016/j.jmps.2003.09.002.

16163028, 2026, 48, Downloaded from https://advanced.onlinelibrary.wiley.com/doi/10.1002/adfm.75699 by Universita Di Ferrara, Wiley Online Library on [23/06/2026]. See the Terms and Conditions (https://onlinelibrary.wiley.com/terms-and-conditions) on Wiley Online Library for rules of use; OA articles are governed by the applicable Creative Commons License

Supporting Information

Additional supporting information can be found online in the Supporting Information section.

Supporting File 1: adfm75699-sup-0001-SuppMat.pdf.

Supporting File 2: adfm75699-sup-0002-VideoS1.mp4.

Supporting File 3: adfm75699-sup-0003-VideoS2.mp4.

Supporting File 4: adfm75699-sup-0004-VideoS3.mp4.

16163028, 2026, 48, Downloaded from https://advanced.onlinelibrary.wiley.com/doi/10.1002/adfm.75699 by Universita Di Ferrara, Wiley Online Library on [23/06/2026]. See the Terms and Conditions (https://onlinelibrary.wiley.com/terms-and-conditions) on Wiley Online Library for rules of use; OA articles are governed by the applicable Creative Commons License